Feasibility of Nano-Acoustic Subsurface Imaging for Atomic Force Microscopy

1st Clayton J. Carlon
School of Engineering
The University of Newcastle
Newcastle, NSW, Australia
Clayton.Carlon@uon.edu.au

2nd Yuen Kuan Yong
School of Engineering
The University of Newcastle
Newcastle, NSW, Australia
Yuenkuan.Yong@newcastle.edu.au

3rd Andrew J. Fleming
School of Engineering
The University of Newcastle
Newcastle, NSW, Australia
Andrew.Fleming@newcastle.edu.au

2025 IEEE International Conference on Mechatronics (ICM) | 979-8-3315-3389-2/25/$31.00 ©2025 IEEE | DOI: 10.1109/ICM62621.2025.10934819

***Abstract*—The feasibility of a new imaging regime for subsurface Atomic Force Microscopy (AFM) is investigated using synthetic aperture focusing technique. This technique uses two Atomic Force Microscopy (AFM) probes to emit acoustic pulses and sense echoes. Unlike other existing subsurface AFM methods, Nano-Acoustic Subsurface AFM (NASAFM) provides cross-sectional images of a sample below the surface with depth information in the nanometre scale. In order to determine the best resolution, two ideal wideband AFM probes are considered in simulation. The results show that a 20 ps pulse with a bandwidth of 330 GHz was able to resolve two 50 nm discs, 500 nm below the surface, separated by 340 nm. Future work is needed to understand the relation between resolution and bandwidth, the optimal imaging parameters, and the sensing technique.**

***Index Terms*—microscopy, atomic force, acoustic, subsurface, imaging, echography, synthetic aperture, beam-forming**

I. Introduction

In semiconductor manufacturing, the quality-control of the fabrication parameters such as layer-thickness and feature-size is achieved by destructively cross-sectioning the device, followed by scanning electron microscopy [1]. This process is wasteful, can only infer the quality over a batch, and adds a delay between the fabrication and quality measurement [2]. To enable real-time quality-control of buried features, subsurface microscopy methods with nanometre scale resolution are in demand.

One subsurface method is scanning acoustic microscopy. These microscopes emit pulses and receive echoes to measure the depth of scattering features and use an acoustic lens coupled on the surface through a liquid [3]. However, the wavelength and the size of the acoustic lens limit the lateral resolution in the micrometre scale [4]. Furthermore, the penetration-depth reduces with higher resolution and frequency.

Depth measurements in the nanometre scale have been achieved with pump-probe lasers in photoacoustic microscopy [5], [6]. Pulses with nanometre wavelengths are emitted and scattered by buried features. Such wave-periods are often in the picoseconds given the high speed of sound in most solids. Although the axial resolution in depth can be achieved at the nanometre scale, the lateral resolution along the surface is limited by the classical diffraction limit and the spot-size of the laser. This resolution is 100 nm to 1 $\mu\mathrm{m}$ [7], [8]. Other methods work around this with either near field optics [9] or acoustic lenses [10], [11].

This project was supported by the Australian Research Council grant DP210103383.

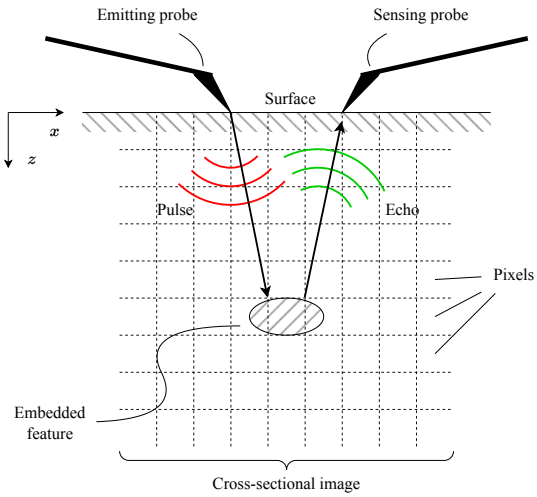

Fig. 1: A basic representation of the subsurface AFM problem.

On the other hand, Atomic Force Microscopy (AFM) achieves lateral resolution in the nanometre scale because of the small tip-size [12]. Although AFM was originally developed to measure the surface topography, there are also opportunities for measuring subsurface properties [13], [14].

The vast majority of subsurface AFM methods rely on inferring mechanical differences through the local elasticity at the surface. This localised measurement can be achieved from either the measured shift in contact-resonance [15], [16] or the force-distance curve inferred from the non-linear mechanical diode effect [17], [18]. A major disadvantage with these methods is that the imaging penetration is only as deep as the stress field of the AFM tip.

To increase the imaging depth, other subsurface methods emit acoustic waves on the underside of the sample which interact with the probe on the top [19], [20]. One of these methods is scanning near-field ultrasound holography which

can resolve gold nanoparticles 15 to 20 nm wide at a depth of 500 nm [21]. However, the sample may need to be cross-sectioned or tampered with to excite waves on the underside. In addition, the feature depth is not directly quantifiable since the estimated depth is indirectly inferred from the local surface properties [22], [23].

In response to this limitation in quantifying depth, optically coupled acoustic AFM methods have been developed that can resolve picosecond acoustic signals. In one such method, an AFM tip was repurposed as a near-field optical probe to sense evanescent waves on the surface [24]. In another method, a pump-laser was applied on the topside of an AFM probe which channelled the nanometre acoustic waves onto the sample through the tip [25]. In a simulation, the thickness of the sample was estimated by the time of flight and speed of sound. These methods open up the feasibility of picosecond pulse-echo measurements with AFM. Despite the promising resolution, an imaging technique is needed to convert the one-dimensional pulse-echo signals to a cross-sectional two-dimensional image.

A. Contributions

A new imaging technique for Nano-Acoustic Subsurface AFM (NASAFM) that utilises time-resolved pulse-echo measurements is proposed to reliably measure the depth and lateral position of buried features. As shown in Fig. 1, a force-pulse is emitted on the surface from an emitting AFM probe, and the resulting echoes are received as surface-deformations by a sensing AFM probe.

A cross-sectional image along depth is constructed as a grid of pixels in Fig. 1. Each pixel's brightness is directly processed from the received signal's amplitude and is correlated to the reflectivity at that location. Thus, the acoustic interfaces between differing materials are imaged.

Since the pulse-wave is spherical and travels across a wide angle, echoes from scattering objects are received from multiple angles. Thus, a method to spatially filter and deconvolve the multiple echoes is needed.

In order to augment the signal processing, the emitting probe repeats a pulse at the same location whereas the sensing probe is moved to a different location. This data-collection process resembles a virtual array of multiple sensing probes. Since the time-scale is in the picoseconds, the repetition of emission-events does not penalise the imaging duration. This configuration allows more advanced signal-processing to enhance the image. As a result, the synthetic aperture focusing technique is utilized to form sharper images than a generic side-scan with a single transducing probe.

This study investigates a theoretical imaging technique as a preliminary step in the future development of NASAFM. Therefore, the imaging method is simulated assuming ideal emitting and sensing probes as a starting point.

As seen in the results, the dual-probe synthetic aperture focusing technique improves the image of single disc compared to a generic single-probe side-scanned image. The lateral resolution is also estimated as 350 nm. However, this can be improved with pulse-compression and anisotropic modelling.

The remainder of the article is as follows. Section II discusses the fundamental acoustic physics which provides estimates of the acoustic speed of sound which is used in the imaging method. Section III explains in detail the synthetic aperture focusing technique method for NASAFM. To test the feasibility of this imaging method, a transient FEA is performed in Section IV on a two-dimensional cross-section with particular emphasis on the lateral resolution. Results and discussions are presented in Section V.

II. Acoustic Theory

Acoustic waves in solids are fundamentally tied to the displacement and elasticity of a particle. The three-dimensional wave equation in a solid is

$$\rho \frac{\partial^2 \vec{u}}{\partial t^2} = (\mu + \lambda)\nabla(\nabla \cdot \vec{u}) + \mu \nabla^2 \vec{u}, \tag{1}$$

where ρ is the density, $\vec{u}$ is the particle's displacement, and μ and λ are the positive Lamé constants related to the stiffness of the solid [26]. Given this equation of motion, the speed for longitudinal waves, where the particle's motion is parallel to the wave's propagation, is

$$V_L = \sqrt{\frac{\lambda + 2\mu}{\rho}}, \tag{2}$$

and the speed equation for transverse waves, where the particle's motion is perpendicular to the wave's propagation, is

$$V_T = \sqrt{\frac{\mu}{\rho}}. \tag{3}$$

Comparing Eqs. (3) and (2), the longitudinal wavefront is faster than the transverse wavefront. Due to the complexity of the geometry and boundary conditions in this work, (1) will be solved numerically using the techniques described in Section IV.

III. Nano-acoustic Imaging

NASAFM has two AFM probes, one as an acoustic emitter and the other as an acoustic sensor. When the former emits a picosecond pulse, the latter detects the scattered waves as vertical surface-deformations. If the emitting probe repeats the same emission at the same location, but the sensing probe is moved to a different location, then the acoustic phenomena should be the identical but sensed at a different location given sufficient time-invariance. This procedure produces the same dataset as a single emitter and an array of sensing transducers. Thus the received echoes can be focused to improve the clarity and resolution. On the other hand, the emitted pulse cannot be directly focused as there is only one emission event at a time.

The synthetic aperture focusing technique can also be used to virtually focus the emitted pulse, for example, in synthetic aperture diagnostic ultrasound [27]. In this reference, there are many receiving elements but only one transmitting element, where each transducer in the array emits a single

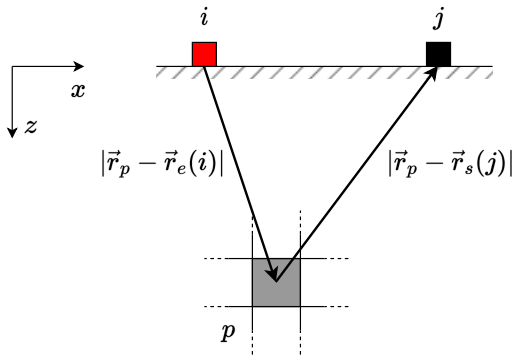

Fig. 2: The path of an emitted wave from the i-th emitter, scattered at the p-th pixel, and then to the j-th sensor.

pulse sequentially. The echo is received by multiple sensing transducers, then back-projected to generate a rough-resolved image. Finally, each of these images are added to form a fine-resolved image.

To investigate the synthetic aperture focusing technique further, an image is drawn as a grid of pixels where the brightness of each pixel represents the reflectivity. This value of reflectivity is directly computed from the received acoustic signal sampled at the time of flight that corresponds to the back-propagated path between the emitter and the sensor. The time of flight of a wave emitted by the i-th emitter, then scattered at the p-th pixel, and received by the j-th sensor in Fig. 2 is

$$t_p(i,j) = \frac{|\vec{r}_p - \vec{r}_e(i)| + |\vec{r}_p - \vec{r}_s(j)|}{c}, \tag{4}$$

where $\vec{r}_e(i)$ is the i-th emitter's position, $\vec{r}_s(j)$ is the j-th sensor's position, $\vec{r}_p$ is the p-th pixel's position, and c is the speed of sound in the medium [27].

The amplitude of the received signal sampled at this time t_p is computed as the reflectivity at the p-th pixel. A high reflectivity corresponds to a scattered echo in the time-domain signal. Therefore, the fully focused reflectivity-image at that given p-th pixel is

$$R_f(\vec{r}_p) = \sum_i \sum_j y_r\left(t_p(i,j), i, j\right), \tag{5}$$

where $y_r(t,i,j)$ is the j-th sensor's received time-domain signal for a single emission from the i-th emitter at time t [27]. Since the received acoustic signals $y_r(t,i,j)$ are measured surface-deformations in the femtometre scale, the units of the reflectivity $R_f(\vec{r}_p)$ are femtometres.

To intuitively understand the synthetic aperture focusing technique more, the inner sum $\sum_j$ of (5) is analogous to a receiving delay-and-sum beam-former given an array of sensors. In addition, the outer sum $\sum_i$ of (5) is analogous to a virtual transmitting delay-and-sum beam-former. Thus, there are two layers of focusing, one receiving and the other transmitting, even though there is only a single emitter each time. These steps are illustrated in Fig. 3.

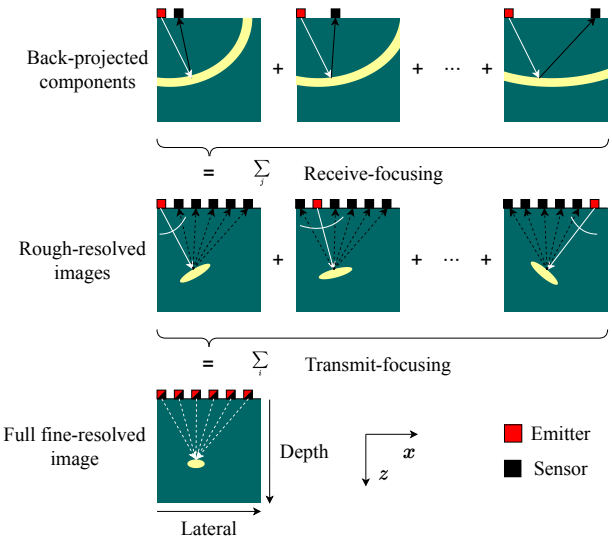

Fig. 3: Process of synthetic aperture imaging.

IV. Simulation Method

Simulations are done through transient FEA in Ansys®Mechanical Enterprise™. A two-dimensional 1 µm-by-1 µm cross-section of a test-sample is simulated to substantially reduce computational time compared to a full three-dimensional model. A mesh of elements is created with element-sizes of 2 nm near the surface, 5 nm near any features, and a default element-size of 20 nm elsewhere. Most of the samples are made of silicon with a copper feature to emulate a semiconductor context. The timestep is 2 ps which gives a simulation bandwidth of 500 GHz.

Surface deformations in the vertical direction are measured on 10 nm wide edges along the surface. A 1 µN pulse force is also applied on one edge at a time. Each of these edges operates as a probing location for either a sensing probe or an emitting probe. Instead of repeating the simulation, multiple sensors are measured for one emission-event. Twenty-six probing locations are 40 nm apart along a 1 µm length. The resolution of the simulated image is 64 by 64 pixels.

The acoustic emission is a 1 µN 20 ps Hann pulse, which results in a bandwidth of 330 GHz. This pulse length is chosen based on the precedent of the acoustic channelling AFM [25] and for achieving a pulse-length of approximately 80 nm in silicon given a longitudinal speed of 8.44 kmh^{-1}.

The surface wave is approximately 100 times higher in amplitude than that of the scattered echoes. As a result, these scattered echoes are difficult to be detected in both the time-domain signal and the image itself. The first preprocessing step is to subtract the reference response from the measurement. The reference response is a pulse-echo measurement, where there are no features.

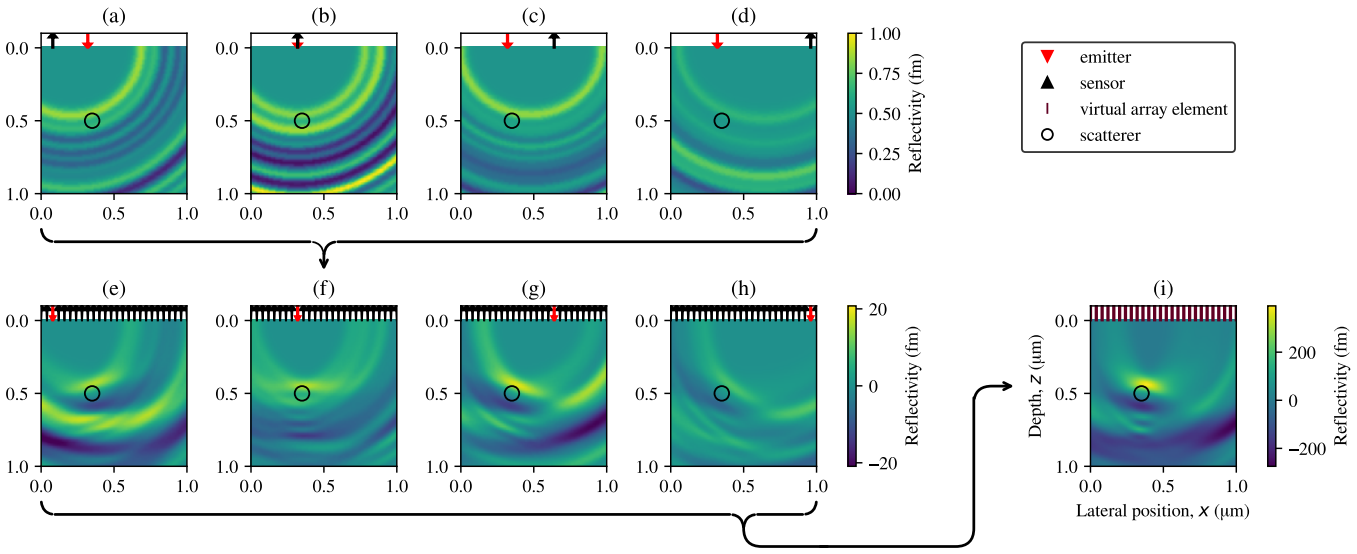

Fig. 4: The NASAFM cross-sectional imaging process of a 100 nm wide copper disc buried in silicon. (a)-(d): back-projected components for a single emitter positioned 320 nm laterally from the left with the sensor positioned at 80, 320, 640, and 960 nm respectively. (e)-(h): the components are then summed into one of these rough-resolved images with the emitter positioned at 80, 320, 640, and 960 nm respectively. (i): the rough-resolved images are then summed further into this fully focused fine-resolved cross-sectional image. Note that only four arbitrary examples are shown in each of the first two rows for simple illustration.

V. Simulation Results

A. Single Disc

The first simulation is an example where a 100 nm copper disc is buried in a silicon plate. An example of a measured acoustic signal in the time-domain is shown in Fig. 5. The received echoes are complex given the multi-path scattering. The impulse on the surface generates both longitudinal and transverse waves. Given that longitudinal waves are the fastest, as shown in Section II, the first peak is the first longitudinal echo.

Back-projection is performed on the received signals for each sensor-emitter pair, which is the innermost term of (5). As seen from the examples in Fig. 4(a-d), each sample of the signal draws an ellipse with the sensor and the emitter as foci. This is expected given that (4) is of the same form as the mathematical definition of an ellipse; that is the sum of the two distances is equal to a constant. The first smaller ellipse corresponds to the first longitudinal echo.

Once these back-projected components are added, the rough-resolved image for a single emission-event is obtained, which corresponds to the inner sum in (5). Examples of the rough-resolved images for a few different emission events are shown in Fig. 4(e-h). As seen in the transformation from Fig. 4(a-d) to Fig. 4(e-h), the blurred spot near the top of the disc is formed by the overlapping of each ellipse corresponding to the first longitudinal echo.

Lastly, all the rough-resolved images are added to form the final fine-resolved image; this is equivalent to the outer sum in (5). From Fig. 4(e-h) to Fig. 4(i), the blurred spots in all the rough-resolved images overlap to form one brighter and sharper spot in the final image.

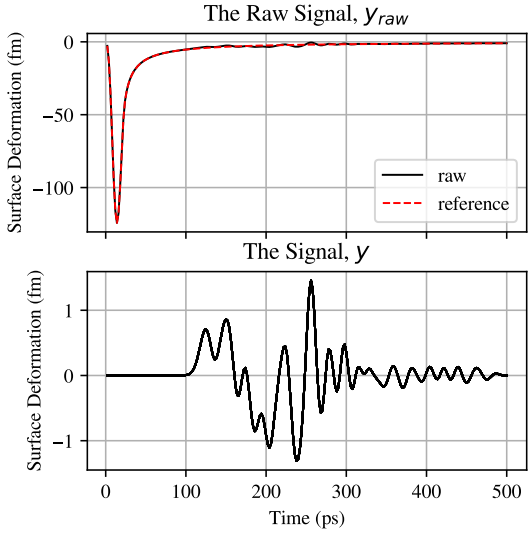

Fig. 5: An example of a received time-domain acoustic signal measured by the vertical surface deformation at a point.

Although there are some artifacts outside the disc, there is still a sufficiently bright spot at the top of the disc where the waves would scatter. Despite the complexity in the received signal in Fig. 5, the synthetic aperture focusing technique removed the secondary echoes and retains the first longitudinal echo. Looking at all these steps, it can be conjectured that

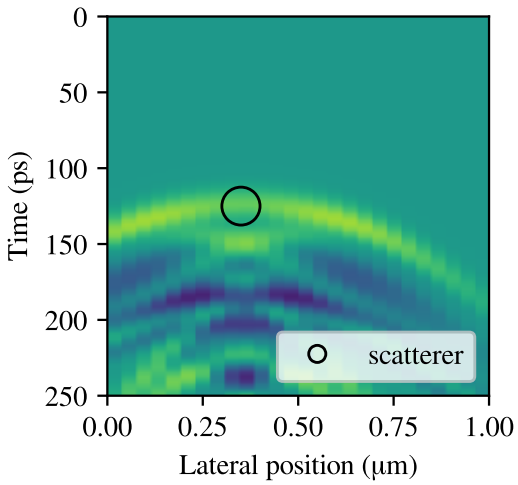

Fig. 6: An alternative image from single emitters and measurements. The disc is drawn at the expected location along the time-axis based on the speed of sound in the material.

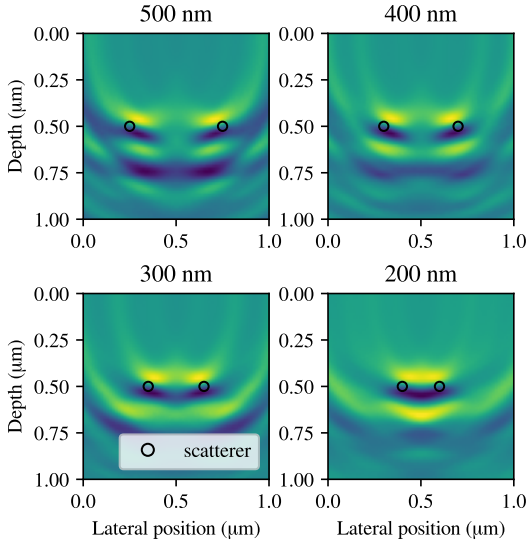

Fig. 7: Two 50 nm wide scattering copper discs set apart at 500, 400, 300, and 200 nm.

sharpness was dependent on the pulse-length of the first echo since the bright spot is an overlapping of the first scattered echo in Fig. 4(a-d).

As a comparison, an alternative image is generated from a single emitting and sensing probe is used, analogous to B-scan medical ultrasound. Each column of pixels is the amplitude of the one-dimensional time-domain signal received at that lateral position. Thus, the image is a series of pulse-echo measurements packed together laterally as side-scans. As seen in Fig. 6, there is a broad undesirable scattering pattern that tapers away from the disc. Furthermore, there is complexity from the secondary echoes beneath the disc. Therefore, between Fig. 4(i) and Fig. 6, the dual-probe method provides improved clarity and simplicity over the single-probe method.

B. Lateral Resolution

The resolution is defined as the shortest distance between two features that can be resolved. Another set of simulations are performed where two 50 nm wide copper discs are moved closer together as shown in Fig. 7. Despite the added complexity of two primary echoes, the two discs are still resolved separately until the bright spots merge together.

To help quantify that lateral resolution, the average of the two brightest peaks is compared with the dimmest spot between the them, referred to as the 'trough'. The trough-to-peak ratio is then calculated for each distance. From Fig. 8, the trough is at 50 % of the average peak at around 340 nm.

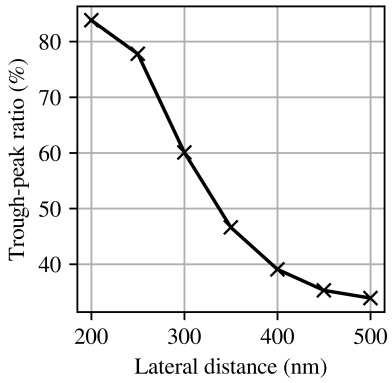

Fig. 8: The trough-to-peak ratio as a percentage versus the lateral distance between two scattering discs.

VI. Conclusion

This article investigates the feasibility of nano-acoustic subsurface imaging with synthetic aperture focusing. Cross-sectional images are achieved in simulation with few artefacts and a lateral resolution of 340 nm. Therefore, subsurface cross-sectional images can be achieved in the nanometre scale given a sufficiently short pulse length.

This imaging method can obtain directly quantifiable depth-information using time-resolved pulse-echo measurements. Unlike existing subsurface AFM methods, it does not rely on surface elasticity to infer the depth of shallow features.

The thicknesses of the ellipses and their overlaying in Fig. 4(a-h) demonstrate that the sharpness of the spot on the disc in Fig. 4(i) is dependent on the width of the first echo. Thus, both the lateral and the axial resolution requires a high bandwidth in the GHz range. Such a high bandwidth is difficult to implement with electronics. The bandwidth requirement can however be relaxed with pulse compression techniques. Future work will include optimising the array size and pulse signal, and investigating methods for emission and sensing.

REFERENCES

[1] A. C. Diebold, *Handbook of Silicon Semiconductor Metrology*. CRC Press, Jun. 2001, google-Books-ID: 9B7e7rNnZPcC.

[2] R. van Gastel, G. Hlawacek, H. J. W. Zandvliet, and B. Poelsema, "Subsurface analysis of semiconductor structures with helium ion microscopy," *Microelectronics Reliability*, vol. 52, no. 9, pp. 2104–2109, Sep. 2012. [Online]. Available: https://www.sciencedirect.com/science/article/pii/S0026271412003277

[3] R. A. Lemons and C. F. Quate, "Acoustic microscope—scanning version," *Applied Physics Letters*, vol. 24, no. 4, pp. 163–165, Feb. 1974. [Online]. Available: https://doi.org/10.1063/1.1655136

[4] F. Bertocci, A. Grandoni, and T. Djuric-Rissner, "Scanning Acoustic Microscopy (SAM): A Robust Method for Defect Detection during the Manufacturing Process of Ultrasound Probes for Medical Imaging," *Sensors*, vol. 19, no. 22, p. 4868, Jan. 2019, number: 22 Publisher: Multidisciplinary Digital Publishing Institute. [Online]. Available: https://www.mdpi.com/1424-8220/19/22/4868

[5] C. Thomsen, J. Strait, Z. Vardeny, H. J. Maris, J. Tauc, and J. J. Hauser, "Coherent Phonon Generation and Detection by Picosecond Light Pulses," *Physical Review Letters*, vol. 53, no. 10, pp. 989–992, Sep. 1984, publisher: American Physical Society. [Online]. Available: https://link.aps.org/doi/10.1103/PhysRevLett.53.989

[6] T. Thréard, E. de Lima Savi, S. Avanesyan, N. Chigarev, Z. Hua, V. Tournat, V. E. Gusev, D. H. Hurley, and S. Raetz, "Photoacoustic 3-D imaging of polycrystalline microstructure improved with transverse acoustic waves," *Photoacoustics*, vol. 23, p. 100286, Sep. 2021. [Online]. Available: https://www.sciencedirect.com/science/article/pii/S2213597921000471

[7] L. V. Wang and S. Hu, "Photoacoustic Tomography: In Vivo Imaging from Organelles to Organs," *Science (New York, N.y.)*, vol. 335, no. 6075, p. 1458, Mar. 2012. [Online]. Available: https://pmc.ncbi.nlm.nih.gov/articles/PMC3322413/

[8] S. Danworaphong, M. Tomoda, Y. Matsumoto, O. Matsuda, T. Ohashi, H. Watanabe, M. Nagayama, K. Gohara, P. H. Otsuka, and O. B. Wright, "Three-dimensional imaging of biological cells with picosecond ultrasonics," *Applied Physics Letters*, vol. 106, no. 16, p. 163701, Apr. 2015. [Online]. Available: https://doi.org/10.1063/1.4918275

[9] P. Siry, L. Belliard, and B. Perrin, "Picosecond Acoustics with Very High Lateral Resolution," *Acta Acustica united with Acustica*, vol. 89, no. 6, pp. 925–929, Nov. 2003.

[10] H. Maris and A. Nurmikko, "Opto-acoustic methods and apparatus for performing high resolution acoustic imaging and other sample probing and modification operations," US Patent US20 060 272 419A1, Dec., 2006. [Online]. Available: https://patents.google.com/patent/US20060272419A1/en

[11] ——, "Enhanced ultra-high resolution acoustic microscope," EP Patent EP2 115 450A4, Mar., 2015. [Online]. Available: https://patents.google.com/patent/EP2115450A4/en

[12] G. Binnig, C. F. Quate, and C. Gerber, "Atomic Force Microscope," *Physical Review Letters*, vol. 56, no. 9, pp. 930–933, Mar. 1986, publisher: American Physical Society. [Online]. Available: https://link.aps.org/doi/10.1103/PhysRevLett.56.930

[13] R. Garcia, "Nanomechanical mapping of soft materials with the atomic force microscope: methods, theory and applications," *Chemical Society Reviews*, vol. 49, no. 16, pp. 5850–5884, 2020, publisher: Royal Society of Chemistry. [Online]. Available: https://pubs.rsc.org/en/content/articlelanding/2020/cs/d0cs00318b

[14] H. J. Sharahi, M. Janmaleki, L. Tetard, S. Kim, H. Sadeghian, and G. J. Verbiest, "Acoustic subsurface-atomic force microscopy: Three-dimensional imaging at the nanoscale," *Journal of Applied Physics*, vol. 129, no. 3, p. 030901, Jan. 2021. [Online]. Available: https://doi.org/10.1063/5.0035151

[15] U. Rabe, "Atomic Force Acoustic Microscopy," in *Applied Scanning Probe Methods II: Scanning Probe Microscopy Techniques*, B. Bhushan and H. Fuchs, Eds. Berlin, Heidelberg: Springer, 2006, pp. 37–90. [Online]. Available: https://doi.org/10.1007/3-540-27453-7_2

[16] K. Y. Kazushi Yamanaka and S. N. Shizuka Nakano, "Ultrasonic Atomic Force Microscope with Overtone Excitation of Cantilever," *Japanese Journal of Applied Physics*, vol. 35, no. 6S, p. 3787, Jun. 1996. [Online]. Available: https://iopscience.iop.org/article/10.1143/JJAP.35.3787

[17] K. Yamanaka, H. Ogiso, and O. Kolosov, "Ultrasonic Force Microscopy for Nanometer Resolution Subsurface Imaging," *Applied Physics Letters*, vol. 64, pp. 178–180, Feb. 1994.

[18] J. D. N. Cheeke, "Mechanical Diode Effect Microscopy," in *Fundamentals and applications of ultrasonic waves*, 2nd ed. Boca Raton: CRC Press/Taylor & Francis Group, 2012, p. 371.

[19] M. T. Cuberes, "Mechanical Diode-Based Ultrasonic Atomic Force Microscopies," in *Applied Scanning Probe Methods XI: Scanning Probe Microscopy Techniques*, B. Bhushan and H. Fuchs, Eds. Berlin, Heidelberg: Springer, 2009, pp. 39–71. [Online]. Available: https://doi.org/10.1007/978-3-540-85037-3_3

[20] M. H. van Es, A. Mohtashami, R. M. T. Thijssen, D. Piras, P. L. M. J. van Neer, and H. Sadeghian, "Mapping buried nanostructures using subsurface ultrasonic resonance force microscopy," *Ultramicroscopy*, vol. 184, pp. 209–216, Jan. 2018. [Online]. Available: https://www.sciencedirect.com/science/article/pii/S0304399117301973

[21] G. S. Shekhawat and V. P. Dravid, "Nanoscale Imaging of Buried Structures via Scanning Near-Field Ultrasound Holography," *Science*, vol. 310, no. 5745, pp. 89–92, Oct. 2005, publisher: American Association for the Advancement of Science. [Online]. Available: https://www.science.org/doi/abs/10.1126/science.1117694

[22] C. Ma, Y. Chen, and W. Arnold, "Contrast Mechanism of Ultrasonic-based Atomic Force Microscopy for Subsurface Imaging," in *2019 IEEE International Ultrasonics Symposium (IUS)*, Oct. 2019, pp. 936–939, iSSN: 1948-5727. [Online]. Available: https://ieeexplore.ieee.org/abstract/document/8925832

[23] M. Hoogesteger, H. Sadeghian, and H. Nijmeijer, "The Sensitivity of Subsurface Contact Resonance Atomic Force Microscopy to Changes in the Depth of Buried Features: a Nonlinear Approach," in *2021 IEEE/ASME International Conference on Advanced Intelligent Mechatronics (AIM)*, Jul. 2021, pp. 110–115, iSSN: 2159-6255. [Online]. Available: https://ieeexplore.ieee.org/abstract/document/9517484

[24] P. Ahn, Z. Zhang, C. Sun, and O. Balogun, "Ultrasonic near-field optical microscopy using a plasmonic nanofocusing probe," *Journal of Applied Physics*, vol. 113, no. 23, p. 234903, Jun. 2013. [Online]. Available: https://doi.org/10.1063/1.4810925

[25] R. Delalande, D. Garcia-Sanchez, and L. Belliard, "Towards acoustic microscopy at the nanoscale by coupling atomic force microscopy with picosecond ultrasonics," *Physical Review B*, vol. 107, Feb. 2023.

[26] J. D. N. Cheeke, "Bulk Acoustic Waves in Solids," in *Fundamentals and applications of ultrasonic waves*, 2nd ed. Boca Raton: CRC Press/Taylor & Francis Group, 2012, pp. 65–79.

[27] J. A. Jensen, S. I. Nikolov, K. L. Gammelmark, and M. H. Pedersen, "Synthetic aperture ultrasound imaging," *Ultrasonics*, vol. 44, pp. e5–e15, Dec. 2006. [Online]. Available: https://www.sciencedirect.com/science/article/pii/S0041624X06003374